Physics of Fluids

Multiscale analysis of the Reynolds stress, dissipation, and subgrid-scale tensor in turbulent bubbly channel flows: Characterization of anisotropy and modeling implications

Cite as: Phys. Fluids **34**, 085122 (2022); https://doi.org/10.1063/5.0104594
Submitted: 20 June 2022 • Accepted: 24 July 2022 • Accepted Manuscript Online: 24 July 2022 • Published Online: 12 August 2022

M. Klein, T. Trummler and J. Radtke

Physics of Fluids ARTICLE scitation.org/journal/phf

Multiscale analysis of the Reynolds stress, dissipation, and subgrid-scale tensor in turbulent bubbly channel flows: Characterization of anisotropy and modeling implications

Cite as: Phys. Fluids **34**, 085122 (2022); doi: 10.1063/5.0104594
Submitted: 20 June 2022 · Accepted: 24 July 2022 ·
Published Online: 12 August 2022

M. Klein,[a] T. Trummler, and J. Radtke

AFFILIATIONS

Department of Aerospace Engineering, University of the Bundeswehr Munich, LRT1, Werner-Heisenberg-Weg 39, 85577 Neubiberg, Germany

[a]Author to whom correspondence should be addressed: markus.klein@unibw.de

ABSTRACT

A direct numerical simulation database of bubbly channel flows at friction Reynolds number 180 and with three different global void fractions has been used to perform a multiscale analysis of the anisotropy of the Reynolds stress tensor, the dissipation tensor, and the subgrid-scale (SGS) tensor in order to characterize the turbulence for a wide range of scales down to the smallest structures occurring in the flow. Based on the hypothesis of Kolmogorov, the non-linear turbulent energy transfer is expected to result in a loss of directional information such that, for a sufficiently high Reynolds number, the small-scale turbulence is expected to be isotropic and universal. The present analysis reveals that the presence of the bubbles increases the anisotropy of the flow which persists down to the smallest scales of motion, even for the dissipation and SGS tensor. This has implications for the complete landscape of turbulence modeling approaches ranging from large eddy simulation, over hybrid approaches to Reynolds averaged Navier–Stokes based modeling.

INTRODUCTION

Kolmogorov,[1] in his first hypothesis, introduced the concept that for a sufficiently high Reynolds number, the small-scale turbulent motions are statistically isotropic,[2] i.e., any statistical quantity is invariant with respect to coordinate axis reflection and rotation. This theory is based on the hypothesis that during the non-linear energy transfer process through the spectrum from large to small eddies, turbulence loses orientation, so that, at sufficiently high Reynolds numbers, the small-scale statistics are isotropic. While this explains the rationale of the large eddy simulation (LES) approach, where only the small, unresolved scales have to be closed, in Reynolds averaged Navier–Stokes (RANS) the whole energy spectrum has to be modeled which requires typically much more complex constitutive equations for the Reynolds stress tensor $\langle u_i' u_j' \rangle$ (here $\langle \cdot \rangle$ denotes a suitable averaging operation and the prime denotes the fluctuating part of velocity) or, alternatively, a Reynolds Stress model which solves for the six Reynolds stress components individually. Because of the scale separation[2] of the turbulent kinetic energy spectrum $E(\kappa)$ with wave number κ (dominant at larger scales) and the dissipation spectrum $D(\kappa) = 2\nu\kappa^2 E(\kappa)$ with the kinematic viscosity ν (dominant at smaller scales), it is often assumed that the dissipation tensor

$$\varepsilon_{ij} = 2\nu \left\langle \frac{\partial u_i'}{\partial x_k} \frac{\partial u_j'}{\partial x_k} \right\rangle \tag{1}$$

obeys an isotropic relation

$$\varepsilon_{ij} = \frac{2}{3}\varepsilon\delta_{ij}, \tag{2}$$

where ε is half the trace of ε_{ij}.

This simple model given by Eq. (2) has sometimes been replaced by a linear relation[3] between the dissipation rate ε_{ij} and the Reynolds stress anisotropies a_{ij}, which is given as follows:

$$\varepsilon_{ij} = \left(\frac{2}{3}\delta_{ij} + C_\varepsilon a_{ij}\right)\varepsilon, \quad a_{ij} = \frac{\langle u_i' u_j' \rangle}{2k} - \frac{1}{3}\delta_{ij}, \quad k = \frac{1}{2}\langle u_i' u_i' \rangle, \tag{3}$$

where C_ε is a coefficient that could be a function of the Reynolds number and goes to zero as the Reynolds number goes to infinity.

An algebraic model for non-isotropic turbulent dissipation has been suggested by Hallbäck *et al.*[4] and Speziale and Gatski[5] in which the Reynolds stress anisotropy is replaced by the dissipation rate anisotropy and the latter quantity is given as

$$e_{ij} = \frac{\varepsilon_{ij}}{2\varepsilon} - \frac{1}{3}\delta_{ij}. \tag{4}$$

Conversely, Liu and Pletcher[6] propose an anisotropic model which approximates the anisotropy tensor a_{ij} using a normalized turbulent dissipation tensor e_{ij}. The relationship between the two anisotropy tensors a_{ij} and e_{ij} has also been explored in Antonia *et al.*,[7] where a linear relation, with a constant of proportionality depending on the local turbulence Reynolds number, has been suggested.

The small-scale turbulence, which is strongly associated with the mechanism of dissipation, has been an active area of research for several decades. It is often studied by analysis of the scaling of the structure functions. An extensive review has been provided by Sreenivasan and Antonia.[8] More recently, Ouellette *et al.*[9] found that the asymmetries of the large-scale flow are reflected in the small-scale statistics of the second-order Lagrangian structure function for high Taylor-scale Reynolds numbers in a laboratory experiment featuring two counter-rotating disks. Pumir *et al.*[10] analyzed the small-scale anisotropy in turbulent channel flows and demonstrated that the statistical properties of the fluctuating velocity gradient in turbulent channel flow are characterized by observables that are insensitive, whereas other quantities are much more sensitive to the anisotropy. Carter and Coletti[11] analyzed the scale-to-scale anisotropy in two facing arrays of randomly actuated air jets. They report a significant departure from isotropy of the moments of the velocity gradients at the dissipative scales. The multiscale behavior of anisotropy occurring in turbulent boundary layers is investigated and analyzed by Liu and Pletcher.[6] The results revealed that the anisotropy does not decay with decreasing scale but persists in the local scales.

Based on the experiments in turbulent shear flow up to a Taylor-scale Reynolds number of $Re_\lambda = 1000$, Shen and Warhaft[12] found that the odd moments of velocity derivatives are non-zero. This contradicts the fact that the small-scale statistics should be invariant to rotation. They conclude that the postulate of local isotropy is untenable on both the dissipation and inertial scales and that this is also unlikely at higher Reynolds numbers. Conversely, Iyer *et al.*[13] reported that independent of the anisotropic content of the energy containing eddies, small-scale turbulent fluctuations recover isotropy and universality faster than previously reported in experimental and numerical studies. They argue that highly anisotropic contributions have not been accurately captured in earlier work.

Independent of the question whether the hypothesis of local isotropy is valid or not, it is at the core of virtually all turbulence theories and models.[13] Sreenivasan and Antonia[8] argue that understanding the small scales will help to parameterize models for both RANS and LES in an appropriate manner.

The flow anisotropy can be conveniently characterized by the properties of the anisotropy tensor a_{ij} (and by analogy for e_{ij}) by analyzing the turbulent state in the so-called Lumley triangle.[14] The boundaries are given in terms of the second II_a and third III_a invariant of a_{ij}

$$II_a = \left(trace(a)^2 - trace(a^2)\right)/2, \quad III_a = \det(a) \tag{5}$$

and by introducing the variables

$$\eta = \left(-\frac{1}{3}II_a\right)^{1/2}, \quad \xi = \left(\frac{1}{2}III_a\right)^{1/3}. \tag{6}$$

Finally, the borders of the Lumley triangle are given by the two straight lines connecting the origin $(0, 0)$ with the points $(-1/6, 1/6)$ and $(1/3, 1/3)$. The third border is represented by the curve $\eta = (\frac{1}{27} + 2\xi^3)^{1/2}$. It can be shown that any physically realizable state of the anisotropy tensors a_{ij} or e_{ij} has to lie within this triangle. These borders of the triangle represent an axisymmetric contraction, axisymmetric expansion, and the two-component state, respectively, while the origin demarks the isotropic state[2] as illustrated in Fig. 1.

It is worth mentioning that Banerjee *et al.*[15] alternatively suggested a barycentric map that provides the possibility of viewing the anisotropic stress tensor, which also offers the possibility of quantifying the weighting for any point inside it, in terms of the limiting states. For convenience, we will use the traditional and more widely known approach.

A considerable amount of research has been conducted to analyze the small scales in isothermal single-phase flows, but CFD applications often cover additional physics. For example, it is known that the energy spectrum of fast rotating turbulence[16] or in quasi-static magnetohydrodynamic turbulence[17] can be anisotropic at all scales. Another example of technical relevance is given by two fluid phases separated by a sharp interface, as discussed in this work. The simulation and modeling of such multiphase flows, such as bubbly flows, have recently been addressed in several works.[18–22] The anisotropy of the Reynolds stress and dissipation tensor in bubbly channel flows of power-law fluids has been analyzed in Ref. 23 in the context of Reynolds averaging. However, today's landscape of computational fluid dynamics (CFD) covers a broad range of methods reaching from conventional one- or two-equation models over hybrid RANS–LES to LES methods, all with varying degrees of fidelity and scale resolving capability. Therefore, it is required to study the anisotropy not only in the context of averaged quantities but also for a varying level of scales reaching from the largest

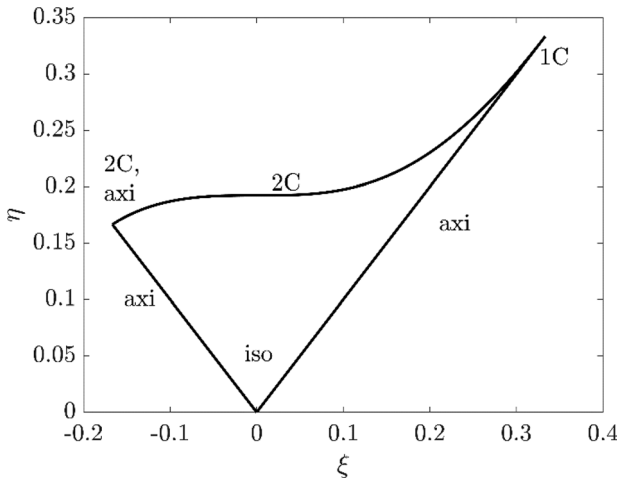

FIG. 1. Sketch of the Lumley triangle and its different turbulent states.

down to the smallest scales. The present work aims to fill this gap in the existing literature by performing a multi-scale analysis of the anisotropy of the Reynolds stress and dissipation tensor in the context of bubbly channel flow for a range of different void fractions. The objectives of the present analysis are (i) to characterize the bubbly flow anisotropy at all scales characteristic of current turbulence modeling approaches, (ii) to provide explanation for the observed behavior, and (iii) to indicate the modeling implications. The rest of the paper will be organized as follows: Methodology section introduces the database and the postprocessing methodology. Then, results will be presented and analyzed before the main findings will be summarized in the conclusions.

METHODOLOGY

This section introduces the numerical solution procedure, the computational setup, and the postprocessing methodology.

Numerical technique and flow configuration

The TBFsolver, developed by Cifani,[24,25] has been used to solve the incompressible Navier–Stokes equation. The solver is well parallelized and is able to handle up to 10^4 deformable bubbles. The finite volume method on a staggered grid is used in conjunction with a QUICK scheme for convective transport and a second-order central differencing scheme for diffusive fluxes. Time integration is performed by a second-order Adams–Bashforth scheme. The Poisson equation is solved by a fast elliptic solver in combination with a modified formulation for the pressure correction after transforming it into a constant-coefficient equation. The liquid–gas interface is described by a volume of fluid method (VOF) and the VOF marker function is advected by a geometrical VOF scheme using a piecewise-linear interface calculation. In order to avoid spurious numerical bubble coalescence, the multi-marker formulation has been applied which assigns a separate volume fraction field to each bubble. The computational domain is a rectangular box of dimension $4\pi\delta \times 2\delta \times 4\pi\delta/3$, where δ is the channel half width, which is resolved by a uniform cartesian grid of dimension $1152 \times 240 \times 384$. The bubbles have been resolved with more than 20 cells per diameter which is considered sufficient for the present configuration.[25] No-slip walls are imposed in the y direction, whereas periodic boundary conditions are used in streamwise (x) and lateral (z) direction. The flow is driven by a constant mass flow, resulting in a wall friction Reynolds number of $Re_\tau = 180$. The liquid to gas density $\rho_l/\rho_g = 20$ and dynamic viscosity ratios $\mu_l/\mu_g = 20$ have been employed. Three cases with different bubble load (low, medium, and high denoted L, M, H in the following) have been simulated together with the single-phase reference channel (S). An overview of the simulation parameters in terms of the number of bubbles N_b, the total (global) void fraction α_{tot}, and bubble Reynolds number Re_b (based on the relative axial velocity of both phases) is given in Table I. In all cases, the bubble diameter d_b, the gravity in mean flow direction, and the coefficient of surface tension are chosen to obtain an Eötvös number of $Eo = (\rho_l - \rho_g)gd_b^2/\sigma = 0.633$. For more details on the numerical solution procedure and computational setup, the reader is referred to Refs. 24–26. Figure 2 exemplarily shows instantaneous snapshots of the liquid–gas interface for cases L, M, and H.

TABLE I. Simulation parameters in terms of the number of bubbles N_b, global void fraction α_{tot}, and bubble Reynolds number Re_b, for the case without bubbles, low, medium, and high void fractions.

Case	N_b	α_{tot}	Re_b
Single (S)	0	0%	N/A
Low (L)	64	0.5%	∼210
Medium (M)	320	2.5%	∼186
High (H)	1280	10%	∼139

Data evaluation

For the multiscale analysis performed in this work, the velocity field has been explicitly filtered using the convolution of two or three 1D Gaussian filter kernels in the following manner (shown here for the three-dimensional convolution):

$$\overline{Q(\boldsymbol{x})} = \int Q(\boldsymbol{x}-\boldsymbol{r})G(r_1)G(r_2)G(r_3)\boldsymbol{dr}, \qquad G(r) = \left(6/\pi\Delta^2\right)^{\frac{3}{2}}\exp\left(-6r^2/\Delta^2\right), \tag{7}$$

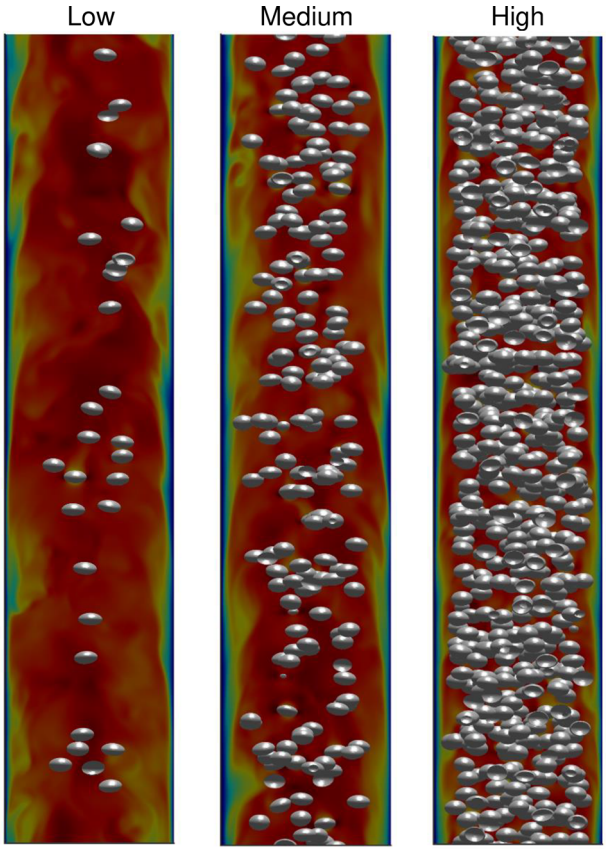

FIG. 2. Instantaneous volume fraction iso-surfaces for cases L, M, and H. It is worth noting that some bubbles intersect with the periodic boundaries, which should not be confused with a concave surface topology.

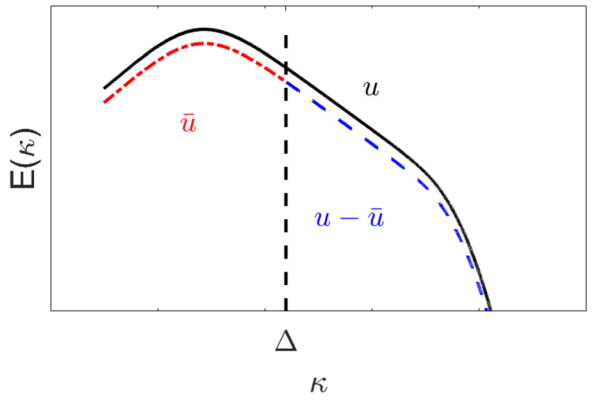

FIG. 3. A sketch of turbulent kinetic energy spectrum of unfiltered velocity u (black line) as a function of wave number in a double logarithmic plot. The red line shows the energy spectrum of the velocity field $\bar{u}$ filtered with a filter of length Δ, while the blue line shows the spectrum of $u - \bar{u}$. For better visibility, the blue and red line are slightly shifted downwards.

where the overbar denotes the filtering operation and Q refers to a general quantity. The application of this convolution integral, corresponding to a lowpass filtering operation, "removes" eddies with size smaller than Δ represented by the filtered velocity field $\overline{\boldsymbol{u}}$. The scales smaller than Δ (associated with a high pass filter of the same filter width) can be obtained by taking the difference $\boldsymbol{u} - \overline{\boldsymbol{u}}$ as illustrated in Fig. 3. For the analysis carried out in this work, a series of filter width has been used corresponding to $n = \Delta/\Delta_{DNS}$, with $n = 2, 4, 8, 16, 32, 50, 64$ and Δ_{DNS} being the direct numerical simulation (DNS) grid spacing.

Filtering in bounded (non-homogeneous) computational domains requires special treatment, whenever the center of the filter approaches the domain boundary, here the wall. Two filter versions are considered and discussed: (i) a two-dimensional filter where filtering is only performed in the periodic $x - z-$ planes, and (ii) a three-dimensional asymmetric filter where the filter kernel is clipped to zero whenever it extends across the bounding wall and the remaining filter kernel is renormalized to unity.

RESULTS

The present configuration represents a bubble laden downflow channel. According to Lu and Tryggvason,[27] the lift force acts to accumulate the bubbles in the channel center. This effect can be clearly seen in the void fraction distribution shown in Fig. 4(a), which results in an increasing flattening of the mean velocity profile with increasing global void fraction [see Fig. 4(b)].

All results in this work are based on one instantaneous flow field and averaging is performed in both homogeneous directions. The results are in very good agreement with those from earlier work which included time averaging on the fly[25] and are considered sufficiently accurate for the qualitative analysis presented in this work. It should also be noted that the profiles shown in Figs. 4–7 have not been averaged over the two channel halves and, consequently, they are not perfectly symmetric. Instead, they provide an indication of the statistical error inherent in the present analysis.

The profiles of the Reynolds stresses in Fig. 5 show the homogenizing effect of the bubbles resulting in an increasingly constant Reynolds stress distribution in the channel center accompanied by peaks in the transition region toward the bubble-free regions close to the walls. By comparing both extreme cases, i.e., the single-phase case and the case with the highest void fraction (10%), it becomes clear that the bubbles increase the homogeneity in the channel bulk flow, but at the same time increase the anisotropy, with a more pronounced dominance of R_{11} over the other components of the Reynolds stress tensor. A more detailed discussion of the first and second order moments can be found in Refs. 24–26 and is not repeated here.

The observations made in Fig. 5 for the Reynolds stresses hold for the dissipation tensor shown in Fig. 6, except that the dissipation peaks at the wall (while $R_{ij} = 0$) and the dominance of ε_{11} over the other components of ε_{ij} is even more pronounced at the wall compared to the Reynolds stresses.

Next, the effects of the two different filter versions (2D vs 3D asymmetric) will be discussed. The results will be shown using a high pass filter with filter sizes $\Delta/\Delta_{DNS} = 2, 16, 32, 64$. The results for intermediate filter sizes follow the same trend and are not shown here for the sake of brevity. In order to be able to relate the filter size to the physical dimensions of the flow, it is recalled that the initially spherical bubbles are resolved with at least 20 cells per diameter, such that the shown filter sizes roughly correspond to $\Delta = 0.1D, 0.8D, 1.6D, 3.2D$, i.e., from scales of about 10% the bubble diameter to more than three times the bubble diameter. It is also important to relate the filter size to the turbulent length scales of the flow. To this end, a directional turbulent length scale is defined in the following manner:

$$L_i = \left(\frac{1}{2}R_{(ii)}\right)^{\frac{3}{2}} \Big/ \left(\frac{1}{2}\varepsilon_{(ii)}\right), \tag{8}$$

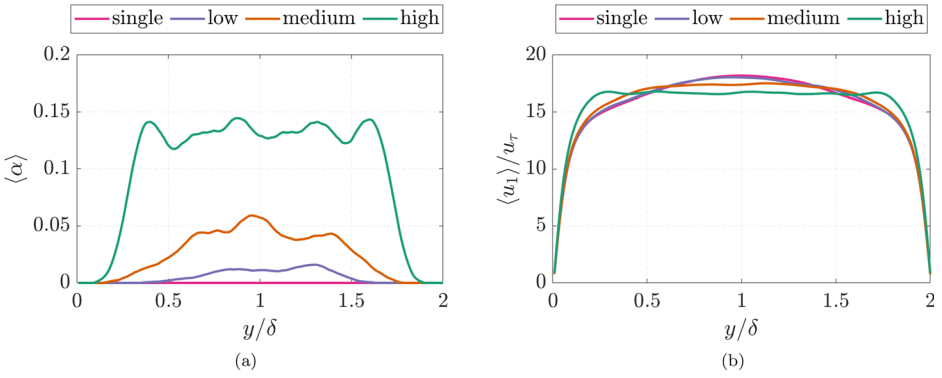

FIG. 4. Profiles of (a) mean gas volume fraction and (b) normalized wall-normal mean axial velocity for all cases.

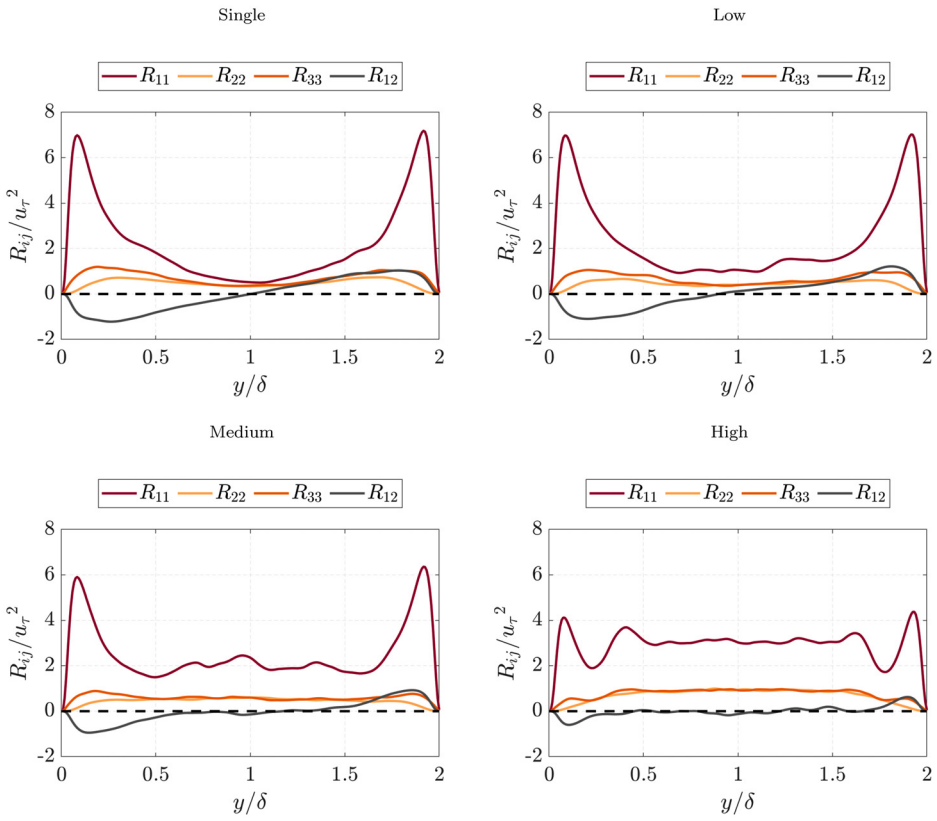

FIG. 5. Normalized wall-normal Reynolds stress profiles for the single-phase flow and the bubbly flows with low, medium, and high global void fractions.

(where the parentheses around the tensor's double indices indicate no summation) in analogy to the traditional definition of the length scale $L = k^{\frac{3}{2}}/\varepsilon = \left(\frac{1}{2}R_{ii}\right)^{\frac{3}{2}}/\left(\frac{1}{2}\varepsilon_{ii}\right)$. This definition is much more convenient than the one based on the integral of the two-point autocorrelation function which requires a very long averaging time for statistics (even longer for bubbly flows, because the small gas fraction needs much larger averaging times) and special treatment if the integrand oscillates or has undershoots. Figure 7 shows the corresponding length scales L_i in all three directions and for the four cases. In all cases, the elongated (streaky) flow structures close to the wall can be clearly seen and this is most pronounced for the single-phase channel flow. The length scales tend to become isotropic toward the channel center for the single-phase case and case L with low global gas fraction. These results are consistent with earlier findings in single-phase channel flows.[23,26]

With increasing void fraction, the length scales decrease because the bubbles act as mixing elements that fragment large flow structures as demonstrated in Refs. 23 and 26. In analogy to the Reynolds stresses, the distribution of turbulent length scales becomes more homogeneous in the bulk flow and also more anisotropic with $L_1 > L_2 \approx L_3$. In summary, it can be noted that the range of Δ/L covers the values that are likely to be observed in LES, hybrid RANS/LES and RANS simulations.

In a next step, the effect of the two different filter kernels will be studied. Figure 8 shows the multiscale analysis of the anisotropy of the Reynolds stresses in the Lumley triangle for all cases and a range of filter width, i.e., $\Delta/\Delta_{DNS} = 64, 32, 16, 2$ from top to bottom. Since a high pass filter is used mostly flow structures smaller than Δ are retained (mostly, because a Gaussian filter is not sharp), and the large energy carrying structures are progressively removed from top to bottom. Note that the point closest to the wall (channel center) is marked with a circle (cross) in Fig. 8 and the subsequent figures. A 2D filter is used for the left column, while a 3D asymmetric filter is used for the right column. It is remarked that very close to the wall the ξ-coordinate changes quickly and the linear interpolation between successive points potentially could give the impression of data points lying erroneously outside the triangle, which is in fact not the case. The general trends observed in Fig. 8 are consistent with available experimental and DNS data from turbulent channel flows:[2] Very close to the wall, in the viscous sublayer of the channel flow, the turbulence is essentially two-component, with v being much smaller than u and w. Anisotropy reaches a peak at a dimensionless wall distance of about $y^+ \approx 7$ close to the 1C state and subsequently becomes increasingly isotropic toward the channel center. While the general behavior is similar for the 2D and the 3D filter, there are remarkable differences close to the wall and the channel center: With the 2D filter, the points close to the wall lie on the curved 2C border at a value of $\xi \approx 0.2$ (or even smaller for smaller filter width), while with the 3D filter these points are shifted toward the 1C end point of the curve. The curved upper border describes the two component state (for channel flow $v' = 0$) with an equality of u' and

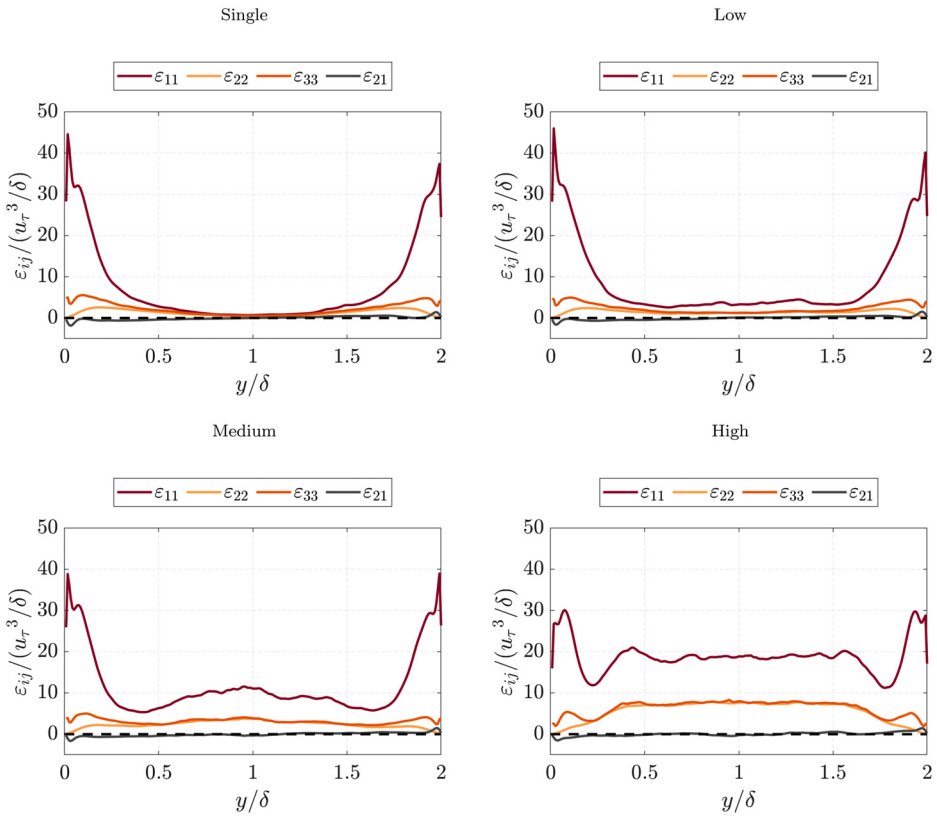

FIG. 6. Normalized wall-normal dissipation profiles for the single-phase flow and the bubbly flows with low, medium, and high global void fractions.

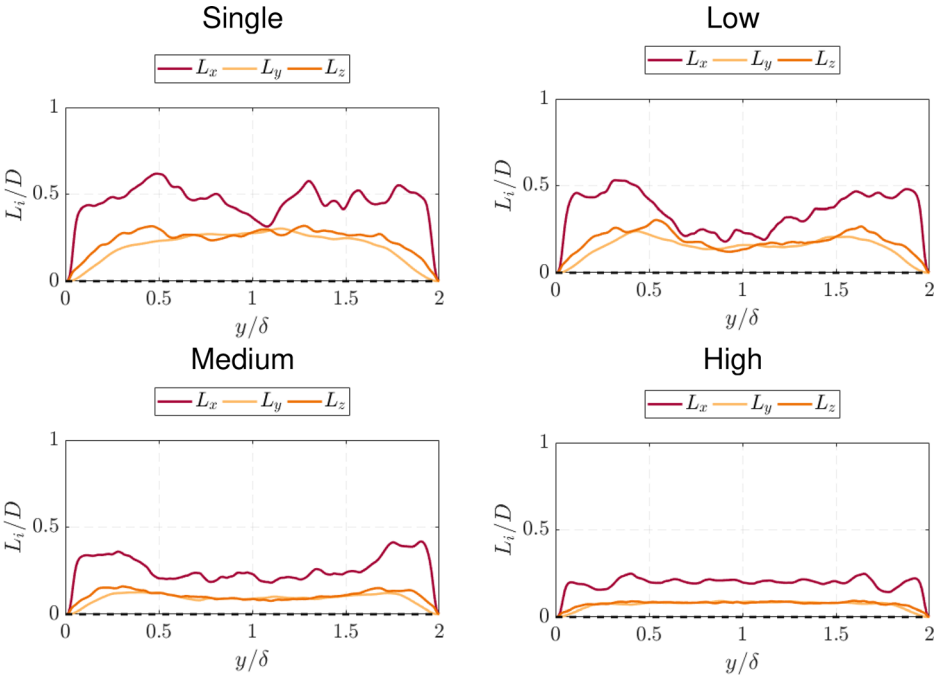

FIG. 7. Directional turbulent length scales normalized with bubble diameter.

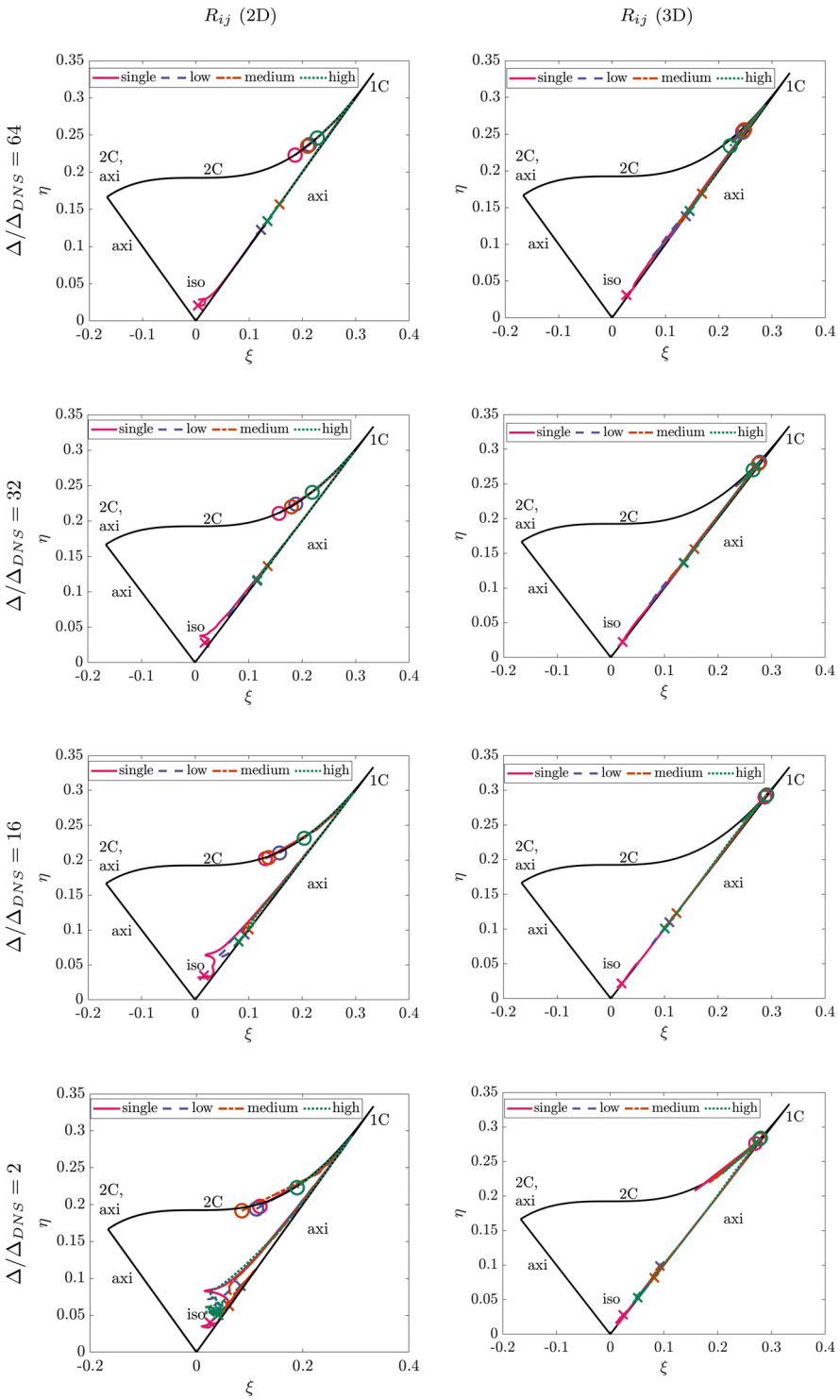

FIG. 8. Multiscale analysis of the anisotropy of the Reynolds stresses in the Lumley triangle for all cases and a range of filter widths. A 2D filter is used for the left column while a 3D asymmetric filter is used for the right column. Here, and in the remaining figures, the point closest to the wall (channel center) is marked with a circle (cross).

w' at the left end (2C, axial) and with $u' \gg w'$ toward the right end (in the 1C limit one has $w' = 0$). Close to the wall one finds[2] $v' \approx 0$ and $u', w' \sim y^{+2}$. However, u' increases much faster than w' (see Fig. 5). At the wall, the 3D filter is asymmetric and, hence, captures higher u' values than w' values. This moves the isotropic state toward the 1C point, because within the filter volume $u' \gg w'$. In contrast, there is no asymmetry effect with the 2D horizontal filter (located in the $x - z$-plane). The energetic structures are elongated in x-direction

(see Fig. 7). If these long streaky structures of axial momentum are filtered away, the axial velocity fluctuations u' will be diminished and will come closer to w', which moves the isotropic state toward the middle of the curved 2C border (see bottom left column). At the channel center nothing unexpected happens for the 3D filter: Things become more isotropic for smaller filter width, which can be seen from the blue, yellow, red, and green crosses moving along the axisymmetric expansion border toward $\xi = 0$. In the channel center, in particular for

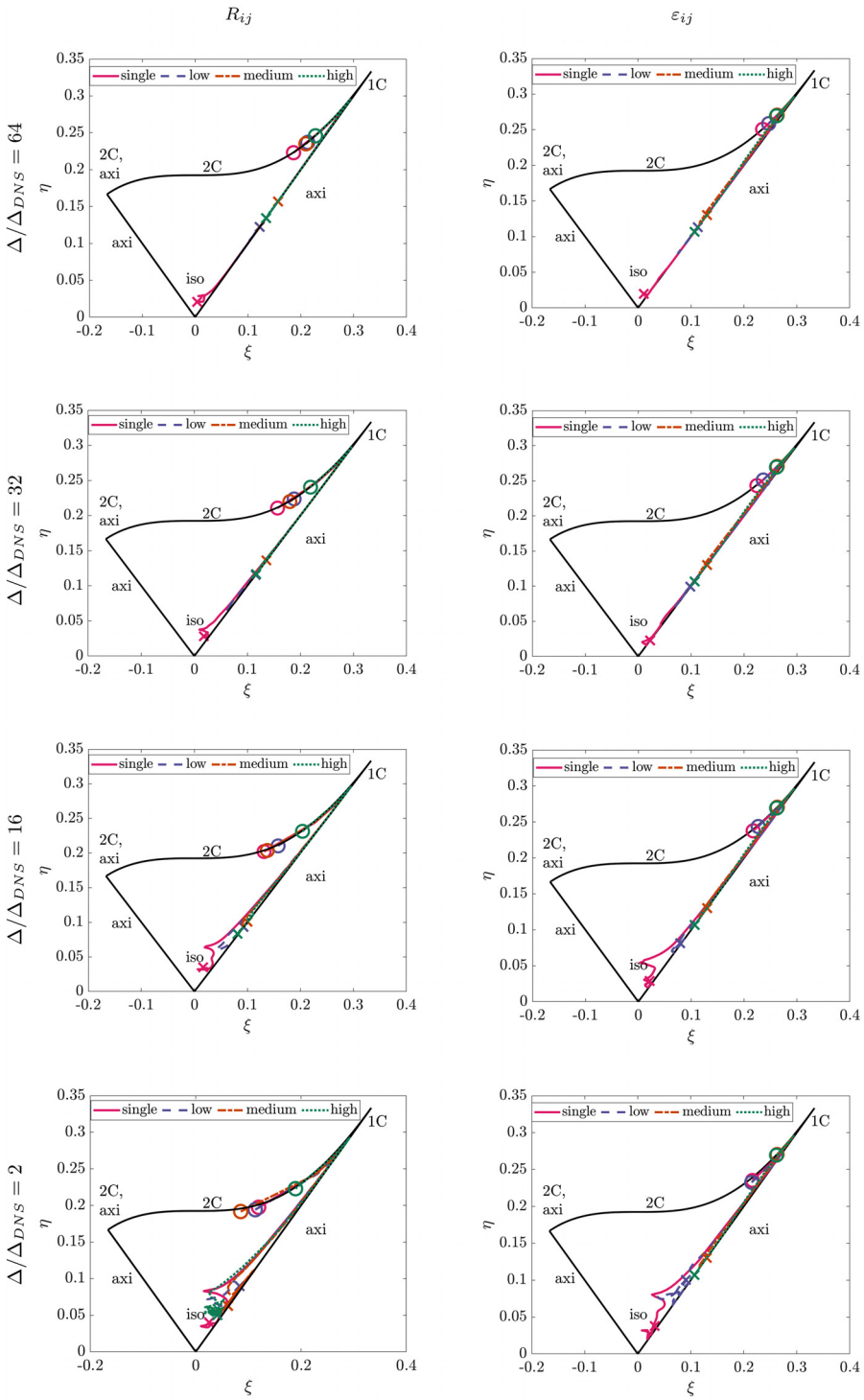

FIG. 9. Multiscale analysis of the anisotropy of the Reynolds stress and dissipation tensors in the Lumley triangle for all cases and a range of filter widths.

the two-phase flow cases, we have $u' > v' = w'$ (axisymmetric compression border). After application of a 2D $x - z$ filter, flow structures in z-direction will have reduced energy content and one obtains $u' > v' > w'$, i.e., a 3D state departing from the axisymmetric border, as can be clearly seen for small filter width.

According to Fig. 8 case M has the highest anisotropy in the channel center. Case M represents a transition between a single-phase channel flow (case S), which resembles case L, and a bubbly flow with high volume concentration, i.e., case H. While the fluctuations increase for all velocity components from case L to case H, the rate of increase

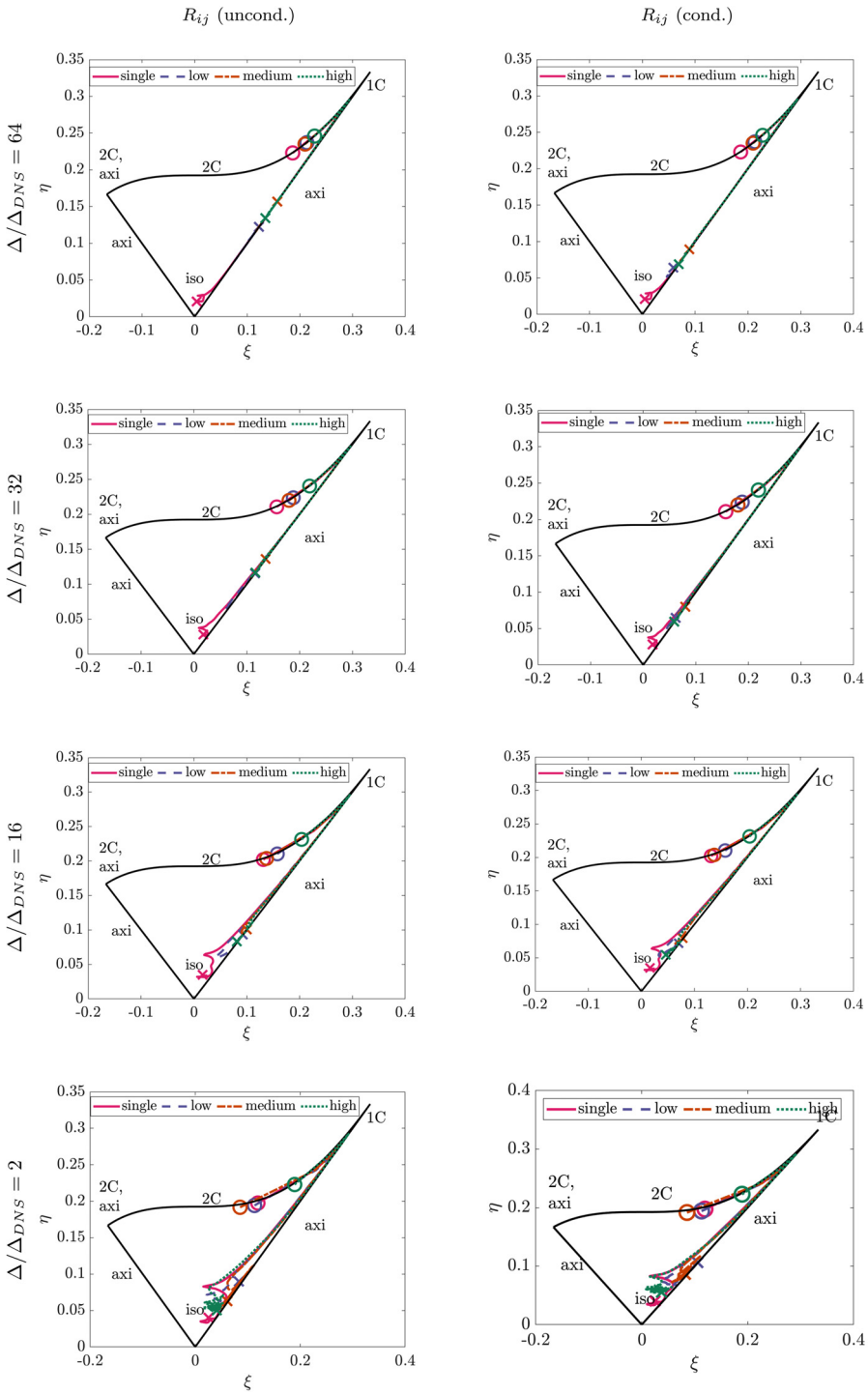

FIG. 10. Multiscale analysis of the anisotropy of the Reynolds stress tensor in the Lumley triangle for all cases and a range of filter widths, based on unconditional velocities (left column) and conditional velocities (right column).

is slower for the velocity components normal to the mean flow direction, resulting in a larger ratio of R_{11}/R_{22} and R_{11}/R_{33}. This behavior is consistent with the Reynolds stress profiles from Cifani *et al.*[25]

The previous discussion reveals that both filtering approaches have some influence on the results obtained. Alternatively, high order commutative filters have been presented in the literature,[28,29] but the commutation property is irrelevant for this kind of *a priori* analysis and the effect of asymmetry will be similar to the filter used in this work. Several classical analyses have employed the 2D filtering approach for *a priori* analysis of single-phase channel flow simulations and the same approach will be followed here for simplicity.[30] All results in the following will henceforth be based on the 2D filter kernel.

Figure 9 shows the multiscale analysis of the anisotropy of the Reynolds stress and dissipation tensors in the Lumley triangle for all cases and four different filter widths. For all filter widths, there is a close coupling between the anisotropies of R_{ij} and ε_{ij}. For the dissipation tensor, the turbulence state at the wall is located closer to the 1C end point compared to the Reynolds stress tensor. Consistent with Figs. 5 and 6, this indicates that close to the wall $\varepsilon_{11}/\varepsilon_{33} > R_{11}/R_{33}$. Furthermore, in both cases, the isotropy increases with decreasing filter size, i.e., as expected the small scales are (slightly) more isotropic. For both tensors, the flow state in the two-phase flow cases is considerably less isotropic compared to the single-phase channel flow as observed in Figs. 5 and 6. Finally, the dissipation tensor is slightly more isotropic than the Reynolds stress tensor which can be seen from the smaller ξ and η coordinates of the endpoints of the curves, which are indicated by crosses. It becomes clear from Fig. 9 that even at the channel center, even for the dissipation tensor and even for the smallest scales a non-negligible anisotropy remains.

All statistics so far have been based on unconditional velocities, i.e., they do not distinguish between velocities of the gas and liquid phase. Classical experimental observations[31] often have been limited to conditional velocities of the continuous, liquid phase. For this reason and for completeness, Fig. 10 compares the anisotropy of the Reynolds stress tensor based on unconditional (left column) and conditional (right column) velocity. Close to the wall, the void fraction approaches zero [see Fig. 4(a)] and the difference between conditional and unconditional Reynolds stresses is small. In the channel center, the two-phase flow tends to be more isotropic when considering conditional velocities compared to unconditional velocities. This is particularly evident for the large filter sizes $\Delta/\Delta_{DNS} \geq 32$, where the two-phase flow features pronounced anisotropies in the channel center. Exemplarily, it is mentioned that the center channel points for the conditional case are all located on the axisymmetric expansion border with values of $\xi \leq 0.15$, whereas for the conditional cases values of $\xi \geq 0.15$ are attained. Since bubbles have been shown to increase

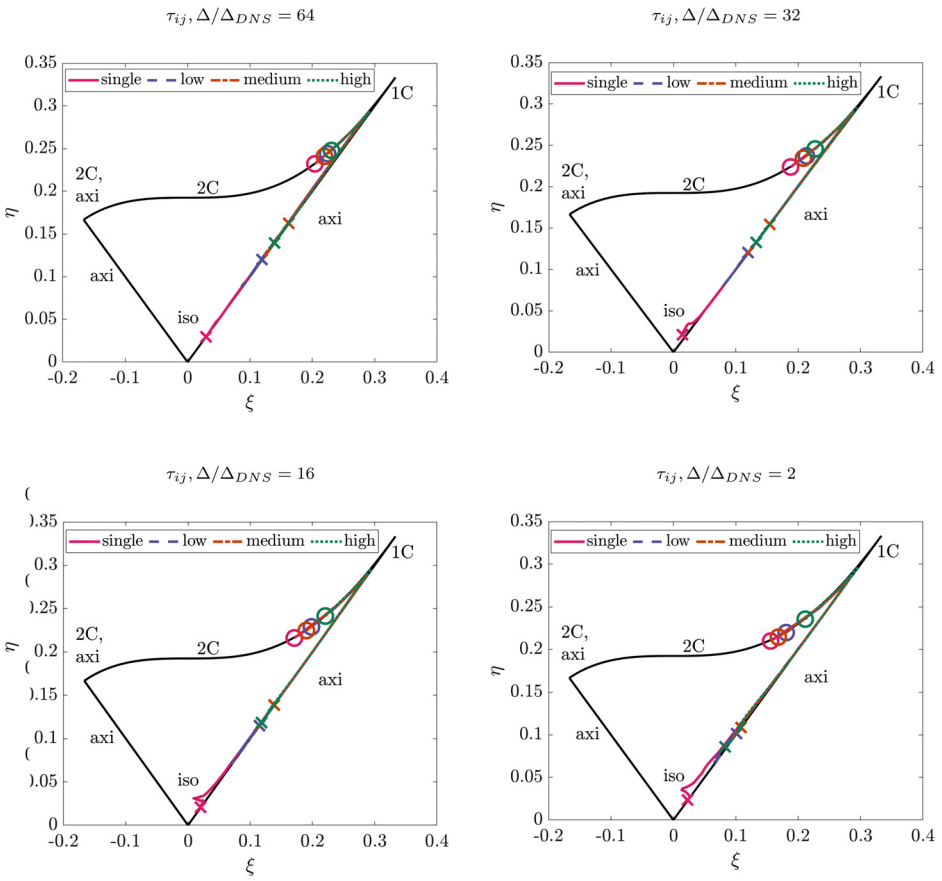

FIG. 11. Multiscale analysis of the anisotropy of the subgrid-stresses in the Lumley triangle for all cases and a range of filter widths.

anisotropy, it is not unexpected that excluding the gas phase leads to moderately increased isotropy. Apart from this, the qualitative findings from earlier figures remain the same for conditional statistics.

Finally, the anisotropy of the subgrid-scale(SGS) stress tensor is analyzed in Fig. 11 for the same filter widths as before. However, in contrast to the previous results, a low pass filter is used to define the subgrid-scale stresses τ_{ij} given by

$$\tau_{ij} = \overline{u_i u_j} - \overline{u_i}\,\overline{u_j}. \tag{9}$$

Once again, it can be seen that the isotropy increases with decreasing filter size, but even for the SGS stresses and the smallest filter size ($\Delta/\Delta_{DNS} = 2$), the anisotropy remains at the channel center in the bubbly channel flows.

CONCLUSIONS

The anisotropy of the Reynolds stress, dissipation, and SGS tensor in a turbulent bubbly channel flow has been characterized using the Lumley triangle. To understand the implications for the full bandwidth of turbulence modeling approaches, which extend more or less continuously from modeling the full energy spectrum in RANS to modeling only the smallest scales in LES, a multiscale analysis has been performed by explicitly filtering the velocity field with a large range of different filter sizes. The smallest (largest) filter width has been selected to be considerably smaller (larger) than the bubble diameter and the energy carrying turbulent structures. The main findings can be summarized as follows:

(i) The presence of the bubbles results in a homogenization of the bulk flow statistics but at the same time increases their anisotropy.
(ii) The same statement holds for the directional turbulent length scales.
(iii) Toward the channel center, the anisotropy decreases moderately with decreasing filter width, where a high pass (low pass) filter is used in the context of RANS (in the context of LES).
(iv) At the wall, the turbulent state of the dissipation tensor is located closer to the one component corner (1C) of the Lumley triangle compared to the Reynolds stress tensor. At the channel center, the dissipation tensor has a slightly larger isotropy.
(v) Conditional and unconditional flow statistics have been compared in terms of their anisotropy. For the present downflow channel configuration, the bubbles stay away from the wall and the conditional averaging affects only the bulk flow region. In the channel center, the conditional statistics tend to be more isotropic than their unconditional counterpart.
(vi) The effect of 2D filtering vs asymmetric 3D filtering has been analyzed and it has been found that the asymmetric 3D filtering influences the Reynolds stress distribution at the wall whereas the 2D filtering results in a deviation from the axisymmetric expansion border toward the channel center for the smallest filter width.

The results show that a non-negligible anisotropy remains even for the dissipation and SGS tensors and even for the smallest scales of motion. This observation is relevant for the modeling of turbulence in two-phase flows across the entire spectrum of methods from LES to hybrid RANS-LES to RANS methods.

As the present analysis is limited to moderate Reynolds numbers, more analysis will be needed in the future to evaluate if the aforementioned trends persist at higher Reynolds numbers.

ACKNOWLEDGMENTS

The authors are grateful to P. Cifani for providing public access to his DNS data.

AUTHOR DECLARATIONS

Conflict of Interest

The authors have no conflicts to disclose.

Author Contributions

Markus Klein: Conceptualization (lead); Data curation (equal); Formal analysis (equal); Funding acquisition (lead); Writing – original draft (lead); Writing – review and editing (equal). **Theresa Trummler:** Data curation (equal); Formal analysis (equal); Software (equal); Supervision (equal); Visualization (equal); Writing – review and editing (equal). **Joseph Radtke:** Data curation (equal); Software (equal); Visualization (equal).

DATA AVAILABILITY

The data that support the findings of this study are available from the corresponding author upon reasonable request.

REFERENCES

[1]A. N. Kolmogorov, "Local structure of turbulence in an incompressible fluid at very high Reynolds numbers," Dokl. Akad. Nauk SSSR **30**, 299–303 (1941).
[2]S. B. Pope, *Turbulent Flows* (Cambridge University Press, 2000).
[3]K. Hanjalic and B. E. Launder, "Contribution towards a Reynolds-stress closure for low-Reynolds-number turbulence," J. Fluid Mech. **74**, 593 (1976).
[4]M. Hallbäck, J. Groth, and A. V. Johansson, "An algebraic model for nonisotropic turbulent dissipation rate in Reynolds stress closures," Phys. Fluids A **2**, 1859–1866 (1990).
[5]C. Speziale and T. Gatski, "Analysis and modelling of anisotropies in the dissipation rate of turbulence," J. Fluid Mech. **344**, 155–180 (1997).
[6]K. Liu and R. Pletcher, "Anisotropy of a turbulent boundary layer," J. Turbul. **9**, N18 (2008).
[7]R. Antonia, L. Djenidi, and P. Spalart, "Anisotropy of the dissipation tensor in a turbulent boundary layer," Phys. Fluids **6**, 2475–2479 (1994).
[8]K. R. Sreenivasan and R. A. Antonia, "The phenomology of small-scale turbulence," Annu. Rev. Fluid Mech. **29**(1), 435–472 (1997).
[9]N. T. Ouellette, H. Xu, M. Bourgoin, and E. Bodenschatz, "Small-scale anisotropy in Lagrangian turbulence," New J. Phys. **8**, 102 (2006).
[10]A. Pumir, H. Xu, and E. Siggia, "Small-scale anisotropy in turbulent boundary layers," J. Fluid Mech. **804**, 5–23 (2016).
[11]D. Carter and F. Coletti, "Scale-to-scale anisotropy in homogeneous turbulence," J. Fluid Mech. **827**, 250–284 (2017).
[12]X. Shen and Z. Warhaft, "The anisotropy of the small scale structure in high Reynolds number ($R_\lambda \sim 1000$) turbulent shear flow," Phys. Fluids **12**, 2976–2989 (2000).
[13]K. P. Iyer, F. Bonaccorso, L. Biferale, and F. Toschi, "Multiscale anisotropic fluctuations in sheared turbulence with multiple states," Phys. Rev. Fluids **2**, 052602(R) (2017).
[14]J. Lumley, "Computational modeling of turbulent flows," Adv. Appl. Mech. **18**, 123–176 (1979).
[15]S. Banerjee, R. Krahl, F. Durst, and C. Zenger, "Presentation of anisotropy properties of turbulence, invariants versus eigenvalue approaches," J. Turbul. **8**, N32 (2007).

[16]M. K. Sharma, M. K. Verma, and S. Chakraborty, "Anisotropic energy transfers in rapidly rotating turbulence," Phys. Fluids **31**, 085117 (2019).
[17]M. K. Verma, "Anisotropy in quasi-static magnetohydrodynamic turbulence," Rep. Prog. Phys. **80**, 087001 (2017).
[18]H. Yan, H. Gong, Z. Huang, P. Zhou, and L. Liu, "Euler–Euler modeling of reactive bubbly flow in a bubble column," Phys. Fluids **34**, 053306 (2022).
[19]E. Laurila, D. Izbassarov, M. Järvinen, and V. Vuorinen, "Numerical study of bubbly flow in a swirl atomizer," Phys. Fluids **32**, 122104 (2020).
[20]D. Lakehal, D. Métrailler, and S. Reboux, "Turbulent water flow in a channel at $Re_\tau = 400$ laden with 0.25 mm diameter air-bubbles clustered near the wall," Phys. Fluids **29**, 065101 (2017).
[21]S. Lin, J. Lu, G. Tryggvason, and Y. Zhang, "A numerical study of oscillation induced coalescence in bubbly flows," Phys. Fluids **30**, 127105 (2018).
[22]A. du Cluzeau, G. Bois, and A. Toutant, "Modelling of the laminar dispersion force in bubbly flows from direct numerical simulations," Phys. Fluids **32**, 012106 (2020).
[23]E. Trautner, M. Klein, F. Bräuer, and J. Hasslberger, "Conditional and unconditional second-order structure functions in bubbly channel flows of power-law fluids," Phys. Fluids **33**, 055121 (2021).
[24]P. Cifani, J. Kuerten, and B. Geurts, "Highly scalable DNS solver for turbulent bubble-laden channel flow," Comput. Fluids **172**, 67–83 (2018).
[25]P. Cifani, J. Kuerten, and B. Geurts, "Flow and bubble statistics of turbulent bubble-laden downflow channel," Int. J. Multiphase Flow **126**, 103244 (2020).
[26]J. Hasslberger, P. Cifani, N. Chakraborty, and M. Klein, "A direct numerical simulation analysis of coherent structures in bubble-laden channel flows," J. Fluid Mech. **905**, A37 (2020).
[27]J. Lu and G. Tryggvason, "Effect of bubble size in turbulent bubbly downflow in a vertical channel," Chem. Eng. Sci. **62**, 3008–3018 (2007).
[28]S. Ghosal and P. Moin, "The basic equations for the large eddy simulation of turbulent flows in complex geometry," J. Comput. Phys. **118**, 24–37 (1995).
[29]O. Vasilyev, T. Lund, and T. P. Moin, "A general class of commutative filters for LES in complex geometries," J. Comput. Phys. **146**, 82–104 (1998).
[30]U. Piomelli, P. Moin, and J. H. Ferziger, "Model consistency in large eddy simulation of turbulent channel flows," Phys. Fluids **31**, 1884–1891 (1988).
[31]M. Lance and J. Bataille, "Turbulence in the liquid phase of a uniform bubbly air–water flow," J. Fluid Mech. **222**, 95–118 (1991).